



HAL
open science

Interest of polarimetric refocused images calibrated in depth for control by vision

Luc Gendre, Stéphane Bazeille, Christophe Cudel, Laurent Bigué

► **To cite this version:**

Luc Gendre, Stéphane Bazeille, Christophe Cudel, Laurent Bigué. Interest of polarimetric refocused images calibrated in depth for control by vision. *Unconventional Optical Imaging*, Apr 2018, Strasbourg, France. pp.68, 10.1117/12.2306939 . hal-03602288

HAL Id: hal-03602288

<https://hal.science/hal-03602288>

Submitted on 9 Mar 2022

HAL is a multi-disciplinary open access archive for the deposit and dissemination of scientific research documents, whether they are published or not. The documents may come from teaching and research institutions in France or abroad, or from public or private research centers.

L'archive ouverte pluridisciplinaire **HAL**, est destinée au dépôt et à la diffusion de documents scientifiques de niveau recherche, publiés ou non, émanant des établissements d'enseignement et de recherche français ou étrangers, des laboratoires publics ou privés.

PROCEEDINGS OF SPIE

[SPIDigitalLibrary.org/conference-proceedings-of-spie](https://spiedigitallibrary.org/conference-proceedings-of-spie)

Interest of polarimetric refocused images calibrated in depth for control by vision

Gendre, L., Bazeille, S., Bigué, L., Cudel, C.

L. Gendre, S. Bazeille, L. Bigué, C. Cudel, "Interest of polarimetric refocused images calibrated in depth for control by vision," Proc. SPIE 10677, Unconventional Optical Imaging, 106771W (24 May 2018); doi: 10.1117/12.2306939

SPIE.

Event: SPIE Photonics Europe, 2018, Strasbourg, France

Interest of polarimetric refocused images calibrated in depth for control by vision

L. Gendre, S. Bazeille, L. Bigué, and C. Cudel

IRIMAS, Université de Haute Alsace,
12 Rue des Frères Lumière, 68093 Mulhouse Cedex, France

ABSTRACT

This work shows the interest of combining polarimetric and light-field imaging. Polarimetric imaging is known for its capabilities to highlight and reveal contrasts or surfaces that are not visible in standard intensity images. This imaging mode requires to capture multiple images with a set of different polarimetric filters. The images can either be captured by a temporal or spatial multiplexing, depending on the polarimeter model used. On the other hand, light-field imaging, which is categorized in the field of computational imaging, is also based on a combination of images that allows to extract 3D information about the scene. In this case, images are either acquired with a camera array, or with a multi-view camera such as a plenoptic camera. One of the major interests of a light-field camera is its capability to produce different kind of images, such as sub-aperture images used to compute depth images, full focus images or images refocused at a specific distance used to detect defects for instance. In this paper, we show that refocused images of a light-field camera can also be computed in the context of polarimetric imaging. The 3D information contained in the refocused images can be combined with the linear degree of polarization and can be obtained with an unique device in one acquisition. An example illustrates how these two coupled imaging modes are promising, especially for the industrial control and inspection by vision.

Keywords: Light-field imaging, polarimetric imaging, surface inspection, refocusing, camera calibration.

1. INTRODUCTION

Both light field and polarimetric imaging need multiple images capture. In this work, we have studied how these two modes can be combined to extract the 3D information and the physical characteristics of objects in the example case of industrial monitoring. Analyzing the polarization of light reflected by objects or surfaces brings a complementary information to what is available with intensity or color imaging. These properties can be used in several domains: To recover specific patterns or targets in a scene¹ or to characterize surfaces composed of different materials when the reflectance intensity captured by a conventional camera on a surface is uniform². The computation of the polarization features requires the acquisition of several images obtained by using different linear or circular optical polarization filters. These images are then used to compute the Stokes vector that describes the whole polarization nature of the light with four elements.

Several polarimeter architectures exist to capture the set of filtered images³, and the imaging polarimeters are classified according to their architecture. The first one is based on the division of amplitude principle, where a light beam is divided in three or four separated channels, each of them equipped with a set of polarizer and camera. Each camera is therefore configured to analyze a specific polarization state of the incoming light beam. This scheme is efficient, but requires a precise mechanical alignment. A second approach is based on the division of time principle: A polarization modulating optical element is placed in front of a single camera that acquires the necessary images successively. This principle is very simple and cheap, unfortunately, the scene must be static to avoid the generation of artifacts due to motion between the frames. Hardware and software solutions to overcome this limitation have been proposed in^{4,5}. A third polarimeter architecture, named division of aperture⁶, consists in acquiring all the polarization data simultaneously using a single sensor. This architecture uses an optical system that divides the incoming beam on four different beams that are then projected all together on one single sensor. In other words, the sensor is divided in four separate areas, each of them measuring

Further author information: Luc Gendre (luc.gendre@uha.fr), Christophe Cudel (christophe.cudel@uha.fr)

a different polarization state. This system allows to acquire all the polarization states simultaneously, but it also requires high quality optical element to ensure that the polarisation is not modified by the beamsplitting element before it is filtered and projected on the sensor. A fourth polarimeter architecture, named division of focal plan⁷, uses a micropolarizer grid placed directly in front of the sensor, like a bayer matrix would be for color measurements. The micropolarizer grid can have different architecture, all of them following the same idea: The image is subsampled at a spacial level. Each pixel measures a different polarization state as its neighbors. This architectures allow very compact systems and high acquisition speed. However, dematrixing algorithm are then necessary to recover the full spatial information and to correct spatial artifacts induces by the micropolarizer grid architecture.

All these previous approaches have been designed to work in 2D imaging mode. In this paper, we will focus on combining this polarimetric information with a 3D information from the light field. Our paper is structured as follows: In Section 2 a state of the art of the domain is introduced, then in Section 3 polarimetric imaging is presented to explain how the degree of linear polarization (*DOLP*) can be obtained with a set of linear filters. In Section 4 we describe the modeling of the acquisition device, and the refocusing process. Next in Section 5, the first results are detailed and we show how the properties of *DOLP* computed in depth can give exploitable information to perform surface inspection. To finish, in Section 6 we give our conclusion and some promising perspectives.



Figure 1: The light field prototype we used for experiments. In its native configuration (left), and with the four additioonnal linear polarizers (0°, 45°, 90° and 135°) mounted in front of each mini-lens (right).

2. STATE OF THE ART

Light-field imaging has been introduced by Lippmann⁸ in 1908, to enhance the photography by proposing a new camera that creates the first 3D photographs. The idea consists in using an array of lenses to capture the intensity and the direction of the light rays, i.e. the light field. In other words we obtain a collection of different point of view of a scene that allows to compute the 3D. We can distinguish two different devices family in the light-field imaging domain. There is the plenoptic camera 1.0, proposed by Andelson⁹ and Ng¹⁰, where light field incoming in a camera is sampled by a micro lens array (MLA) placed between the image sensor and the main lens. In this case, the MLA is placed in the image plane of the main lens. The plenoptic image obtained is a 2D array of 2D arrays that encodes the position and orientation of the light rays. Another principle, consists in capturing a series of points of view. This can be realized in three different ways. Firstly, the images can be obtained sequentially with a coded aperture mask placed in an objective optical way¹¹. Secondly, the images can be obtained simultaneously by aligning a set of cameras¹². Finally, the images can also be obtained by splitting the image plane of a single camera in several points of view. This last principle has been introduced by Lumsdaine and Georgiev¹³ with the name focused plenoptic camera. For each model of the light-field camera, the raw data collected can be used to produce a remarkable wide variety of images: The sub-aperture images that are a collection of synthetic points of view; the epipolar images that are used to compute a depth map

or a disparity image; a full focused image or a stack of refocused images. The refocused capability of light-field or plenoptic cameras is well known. Its principle¹⁴ consists in computing a virtual plane where light rays are intersecting. According to the nature of light-field devices, this is realized by rearranging raw images, or integrating light-rays in the spatial or the frequency domain. It has to be noted that refocused images are interesting to produce artistic effects on digital photographs or in the cinema industry as it is described by the Lytro company¹⁵. In other domains, refocusing can also be used to recover the depth of a scene as in¹⁶ for example. In 2011, Georgiev *et al.*¹⁷ revisited the definition of the plenoptic function and introduced the term of Rich Image Capture (RIC). Instead of capturing only the intensity of the light-field, two spatial allocation approaches are proposed by using neutral density or polarimetric filters to capture also information about the radiance. Both schemes lead to compute HDR images or images where arbitrary polarization angles can be chosen. For instance, Horstmeyer *et al.*¹⁸ presented a single shot multispectral camera based on a pinhole array. More recently, other approaches have been proposed to combine light-field and polarimetric imaging. In¹⁹ the authors select the pixels that will contribute to 3D reconstruction depending on a criteria related to the degree of polarization. Another work has been proposed by Carnicer *et al.*²⁰ dedicated to low illumination scene where the degree of polarization is difficult to obtain with conventional method. By translating a camera, photons are counted, and a maximum likelihood estimation is used to retrieve the 3D and compute in a second step the degree of polarization. In this paper, we develop another approach that could be used with any light field camera with refocusing capabilities. We used our own camera prototype constituted of four mini-lenses to obtain four sub-images on a single camera sensor. In²¹, we created for this device a method to generate a stack of refocused images at a precise distance. We have also shown how these refocused images can be used to perform enhanced visual inspection. We modified this camera prototype by adding a set of four linear polarimetric filters (see Fig. 1), and we propose to combine refocused images with the *DOLP* in order to analyze objects surfaces extracting informations such as the presence of a defect and its 3-D location.

3. POLARIZATION FORMALISM

The formalism we will use to describe the polarization state of a light beam is the Stokes formalism²². Polarization light beam characteristics are gathered in a four components vector \mathbf{S} described in Eq. 1.

$$\mathbf{S} = \begin{bmatrix} s_0 \\ s_1 \\ s_2 \\ s_3 \end{bmatrix} \quad (1)$$

where s_0 represents the light intensity that would be measured by a sensor not sensitive to polarization, s_1 expresses the polarization oriented at 0° or 90° from the angular reference, s_2 is the polarization oriented at 45° or 135° , and s_3 the right- or left-handedness of the polarization. This Stokes vector can be estimated from intensity measurements operated by a sensor placed behind a polarizer oriented at specific angles²³ as detailed in Eq. 2.

$$\mathbf{S} = \begin{bmatrix} s_0 \\ s_1 \\ s_2 \\ s_3 \end{bmatrix} \propto \begin{bmatrix} (I_0 + I_{90}) \text{ or } (I_{45} + I_{135}) \text{ or } (I_0 + I_{90} + I_{45} + I_{135})/2 \\ I_0 - I_{90} \\ I_{45} - I_{135} \\ I_r - I_l \end{bmatrix} \quad (2)$$

where $I_{i, i \in \{0, 45, 90, 135\}}$ is the light intensity measured through a linear polarizer oriented at an angle i , and where I_r (resp. I_l) is the light intensity measured through a right (resp. left) circular polarizer. From Eq. 2, one can understand that a system that does not include circular polarizers or other circularity sensitive components, such as wave-plates other than half wave-plates for example, will not be able to provide measurements to estimate the s_3 component. This is our case in this paper. As we explained in the previous section, our system only integrates four linear polarizers. As a consequence, s_3 remains unknown and will not be mentioned any further in the paper. We will focus on metrics that can be evaluated only from the first three components of the Stokes vector: s_0 , s_1 , and s_2 . One metric that will be computed from the estimated Stokes vector is the Degree of

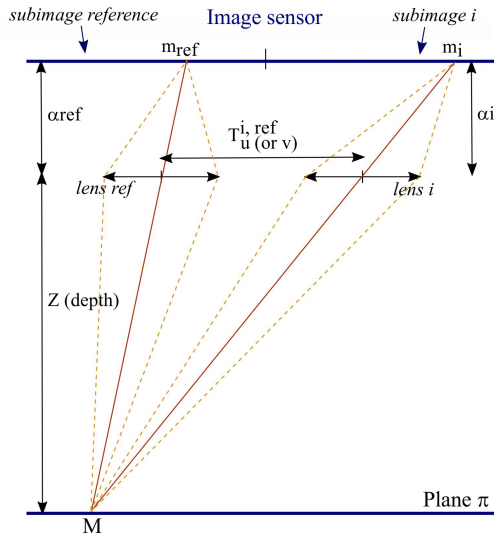


Figure 2: 2D representation of the light field camera.

Linear Polarization (*DOLP*). It quantifies the amount of light that is actually polarized with respect to the overall light beam. It takes values from 0 for unpolarized light to 1 for totally polarized light, intermediate values referring to partially polarized light. The *DOLP* is related to the Stokes vector as expressed in Eq. 3.

$$DOLP = \frac{\sqrt{s_1^2 + s_2^2}}{s_0} \quad (3)$$

4. MULTI-VIEW CAMERA, CALIBRATION AND REFOCUSED IMAGES

This work is based on a multi-view camera prototype developed in our laboratory (see Fig. 1 and 2). We have modified the front panel of an industrial camera to replace the C mount panel by a new one able to support 4 mini-lenses. Each mini-lens has a diameter of about 8 mm. The baseline between each mini-lens gives 4 different points of view of the scene, which are used to extract the 3D information. As the baseline is much smaller than the one encountered most of the time in standard stereo-vision, the depth working distance is limited. We have estimated that our device is qualified to work on a range of depth defined between 20 cm and 1.5 m. On a second step, we have placed a set of linear polarimetric filters in front of each mini-lens (see Fig. 1.b). In a previous work²¹, we have studied the calibration of this device in order to generate refocused images calibrated in depth. We have shown the advantages of working with a stack of refocused images for the control in industrial vision. In particular, we have demonstrated that it is possible to highlight areas of the image at a known depth while blurring all other parts of the image with a defocused effect. We have also studied how depth can be measured by analyzing the gradients following the depth dimension in a stack of refocused images.

4.1 Camera modeling

We use a set of homographies defined between each view to perform the calibration of our device. Then we can generate a stack of refocused images at any depth, from a single acquisition. On Fig. 2 we show the geometry of our prototype. We define arbitrarily one view, as being the reference image noted I_{ref} and we designate by I_i any of other sub-image i . Any point M of the plane π is projected with homographies H_{ref} and H_i in the sub-images ref and i . These first terms allow to define the homography $H_{ref,i}$ to establish a relation between the projections m_{ref} and m_i of any point M of plane π in images I_{ref} and I_i :

$$m_{ref} = H_{ref}.H_i^{-1}.m_i = H_{ref,i}.m_i \quad (4)$$

Any homography H_i (including H_{ref}) is defined as being the product between an intrinsic matrix A_i and a projection matrix $P_{i,ref}$, with

$$A_i = \begin{pmatrix} \alpha_{ui} & 0 & u_{i0} \\ 0 & \alpha_{vi} & v_{i0} \\ 0 & 0 & 1 \end{pmatrix}, P_{i,ref} = \begin{pmatrix} 1 & 0 & T_u^{(i,ref)} \\ 0 & 1 & T_v^{(i,ref)} \\ 0 & 0 & Z \end{pmatrix}, \quad (5)$$

with α_{ui} and α_{vi} the horizontal and vertical focal lengths, (u_{i0}, v_{i0}) the image center, Z the depth of plane π and $(T_u^{(i,ref)}, T_v^{(i,ref)})$ the translations between optical center of sub-images I_{ref} and I_i . These expressions lead to write $H_{i,ref}(Z)$ with the intrinsic and extrinsic parameters of the system that can be expressed with the following constant terms A_u, A_v, B_u, B_v, C_u and C_v .

$$H_{ref,i}(Z) = \begin{pmatrix} \frac{\alpha_{ui}}{\alpha_{uref}} & 0 & u_{i0} - \frac{\alpha_{ui}}{\alpha_{uref}} \cdot u_{0ref} - \frac{\alpha_{ui} \cdot T_u^{(i,ref)}}{Z} \\ 0 & \frac{\alpha_{vi}}{\alpha_{vref}} & v_{i0} - \frac{\alpha_{vi}}{\alpha_{vref}} \cdot v_{0ref} - \frac{\alpha_{vi} \cdot T_v^{(i,ref)}}{Z} \\ 0 & 0 & 1 \end{pmatrix} = \begin{pmatrix} A_u & 0 & B_u - \frac{C_u}{Z} \\ 0 & A_v & B_v - \frac{C_v}{Z} \\ 0 & 0 & 1 \end{pmatrix}, \quad (6)$$

Based on this model, we have proposed a rapid calibration, in two steps, in order to determine the constant terms. Calibration is done by using a chessboard that must be placed parallel to the image sensor for each step. Firstly, the chessboard pattern is placed at a known depth Z_{cal} that is considered as the first calibration distance. The set of homographies $H_{ref,i}(Z_{cal})$ are then computed with the set of corners detected on each sub-image. Secondly, the chessboard pattern is shifted to a known depth $k \cdot Z_{cal}$ and homographies $H_{ref,i}(k \cdot Z_{cal})$ are again computed. Basically, this second depth can be 70 or 80% of the Z_{cal} depth, but must be known precisely. Numerical values of homographies are then used for determining the constant terms A_u, A_v, B_u, B_v, C_u and C_v . Subsequently, after calibration, any homography $H_{ref,i}(Z)$ can be fully determined for any working depth Z .



Figure 3: Refocused images obtained at specific defined depths (Z). (right) : Image refocused on the top of object ($Z = 314$ mm); (center): Image refocused on the bottom ($Z = 432$ mm); (left) : Examples of depth computed on the three regions of interest surrounded in green. The depths have been obtained by scanning a stack of 100 refocused images which have been generated with a depth step of 1 mm.

4.2 Refocused images

The digital refocusing is one characteristic of light-field imaging. Whatever the model of light field camera and the corresponding algorithms used, one can say that refocused images are usually obtained by some combinations of addition or average operators. For instance, in the case of camera plenoptic 1.0, the refocused images are computed by adding the light rays in virtual plane that is located in front or behind the image sensor. For the focused plenoptic cameras or camera array, the refocused images are obtained by adding some points of view

captured by the device. In our own case, the refocused images are obtained by summing the projections of each sub-images in the coordinate system of the reference image, by using the set of homographies $H_{ref,i}(Z)$,

$$R(Z) = \frac{1}{N} \cdot \sum_{i=0}^{N-1} H_{ref,i}(Z) \cdot I_i \quad (7)$$

where N represents the number of sub-images of the device. $N = 4$ in our case. Overviews of some refocused images computed for two depths Z are given on Fig. 3. This figure gives also an example of 3D capabilities of refocusing. On this image, the depths are obtained by comparing a reference ROI (region of interest) to the ones in a stack of refocused images, generated over a range of 30 cm in depth. When the matching score is optimal, each ROI is assigned at the depth of the corresponding refocused image index.

4.3 Refocused images with linear polarimetric filters

There is an interesting relation in Eq. 2 where s_0 is the total intensity of light incoming to the system, and can be assimilated to the conventional image acquired without any polarimetric filter. By definition:

$$s_0 = \frac{1}{2} \cdot (I_0 + I_{45} + I_{90} + I_{135}) \quad (8)$$

So when the sub-images captured by the camera are optically aligned, the stokes parameters can directly be computed with Eq. 2. Therefore, by using the refocusing principle of our light field camera to align the point of views following Z , we are able to compute a stack of the three first Stokes parameters such as:

$$\mathbf{S}(Z) = \begin{bmatrix} s_0(Z) \\ s_1(Z) \\ s_2(Z) \end{bmatrix} \propto \begin{bmatrix} \frac{1}{2} \cdot \sum_i H_{ref,i}(Z) \cdot I_i, \text{ where } i \in \{0, 45, 90, 135\} \\ H_{ref,0}(Z) \cdot I_0 - H_{ref,90}(Z) \cdot I_{90} \\ H_{ref,45}(Z) \cdot I_{45} - H_{ref,135}(Z) \cdot I_{135} \end{bmatrix} \quad (9)$$

By extension, the Degree Of Linear Polarization can also be described with the following definitions of the stacks $DOLP(Z)$:

$$DOLP(Z) = \frac{\sqrt{s_1^2(Z) + s_2^2(Z)}}{s_0(Z)} \quad (10)$$

Thanks to the polarimetric filters, the light-field camera becomes a polarimeter device, where the measurement of the Stokes vector and the degree of linear polarization are related to the depth of objects or surfaces analyzed by the camera. Several methods can be applied or developed to combine the depth by using the refocused images and the polarimetric information. In this study, we have focused our work on the inspection of uniform surfaces. We contracted on the task of detecting and locating the depth of defects on an object. In the next section, we will show how histograms can be computed on region of interest of $DOLP(Z)$ images and used to characterize three situations : Uniform surface, appearance of defect when the surface is damaged, or appearance of defect due to impurity that has accumulated on the surface.

5. EXPERIMENTS AND RESULTS

5.1 Experimental Setup

The experimental setup (see Fig. 4) is constituted of a scene illuminated with a polarized ring light placed around the camera. Two wooden panels were placed at different distances Z_1 and Z_2 with respect to the camera. The samples were laser machined to change their surface aspect without modifying the nature of the material (no coating was added on top of the samples). Stripes of various depth have also been added in each sample.

From this configuration, a single image is acquired and divided in four sub-images corresponding to the four lenses on the system. An example of these four images is presented on Fig. 5. In a second step, assuming the calibration has been previously performed²¹, we generate the stacks $s_0(Z)$, and $DOLP(Z)$, as explained in section 4.1. Fig. 6 presents an example of $s_0(Z)$ and $DOLP(Z)$ images for a depth Z chosen as focused on the top sample. This video (available with online version of the article) associated with this figure shows clearly the

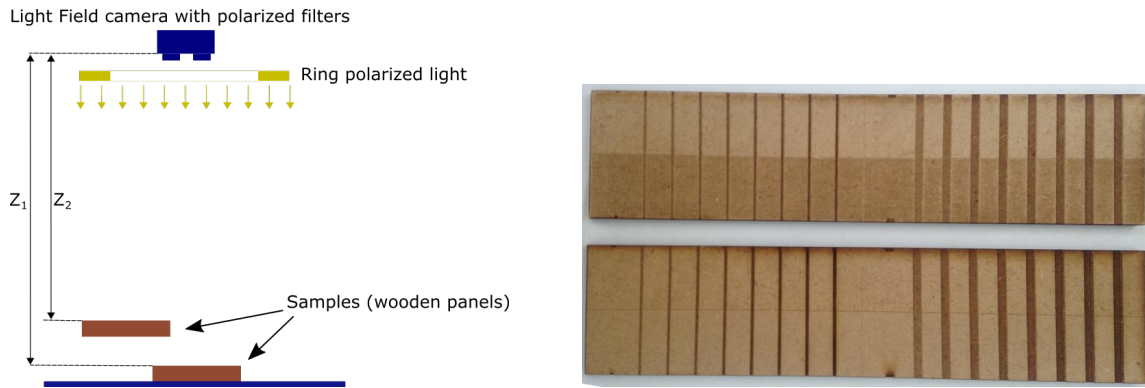


Figure 4: Experimental setup. Left: Drawing of the experiment. Right: Laser-marked wood samples.

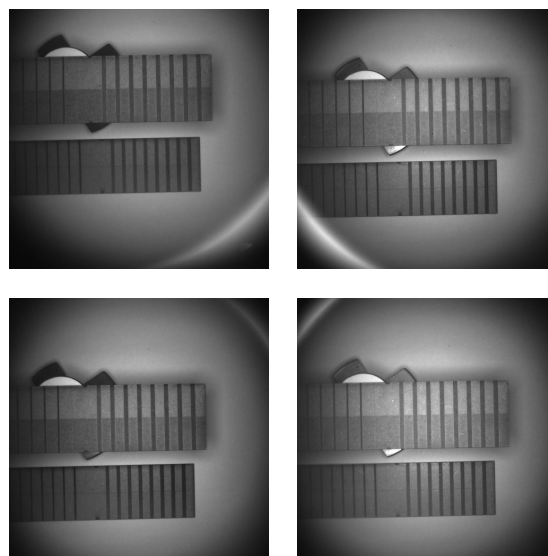


Figure 5: The four raw images extracted from a single snapshot image acquired by the system

complementary information provided by $s_0(Z)$ and $DOLP(Z)$ when the depth Z varies. $s_0(Z)$ corresponds to the stack of refocused intensity images without the polarization information, while $DOLP(Z)$ gives the calculated degree of polarization (using Eq. 9 and 10) exclusively for the areas which are well refocused. This is clearly visible on the parts where there are vertical stripes that have been machined by a laser beam. These stripes disappear completely on the refocused images computed for the depths $Z = Z_1$ and $Z = Z_2$, corresponding to Z -location of the samples analyzed. The $DOLP(Z)$ is then homogeneous on the whole surface of tested samples, whatever the nature of laser stripes on the surface. Outside of these values of Z , the resulting $DOLP(Z)$ is a combination of mismatch alignments of Stokes vectors. This produces larger objects edges on the $DOLP$ picture. It is an interesting property which can be used to evaluate both depth and degree of polarization from a stack of computed refocused images.

5.2 Stripes characterization based on Degree of Linear Polarization

Based on the property stated above, we will present our results obtained from a stack of refocused $DOLP(Z)$ images. First, we consider the $DOLP$ image that is refocused on the upper wooden sample on Fig. 7. This upper sample is located at a distance Z_1 closer to the camera than the second sample. On this picture, we compared the $DOLP$ histogram of two ROIs placed on similar stripes on the two wooden samples. As it can be seen Fig. 7, the histogram of the upper sample is clearly narrower than the other one.

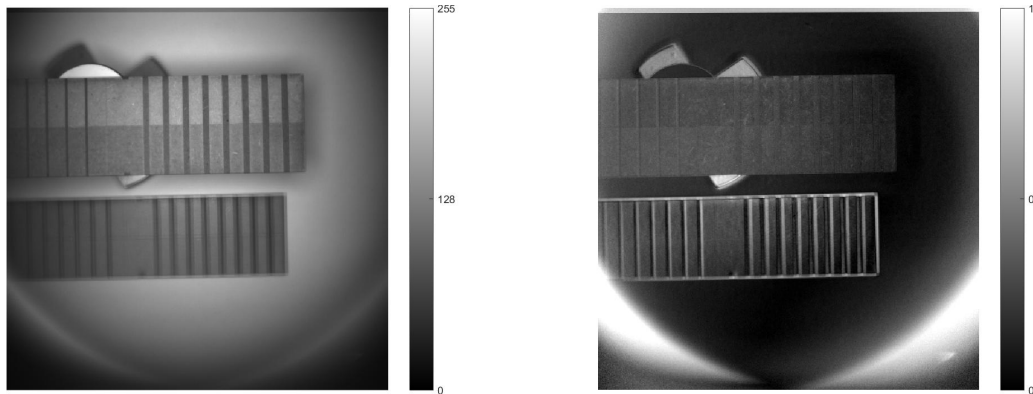


Figure 6: Video1 (online version) showing examples of s_0 (left) and $DOLP$ (right) images as computed from raw data acquired by the system. <http://dx.doi.org/10.1117/12.2302592>

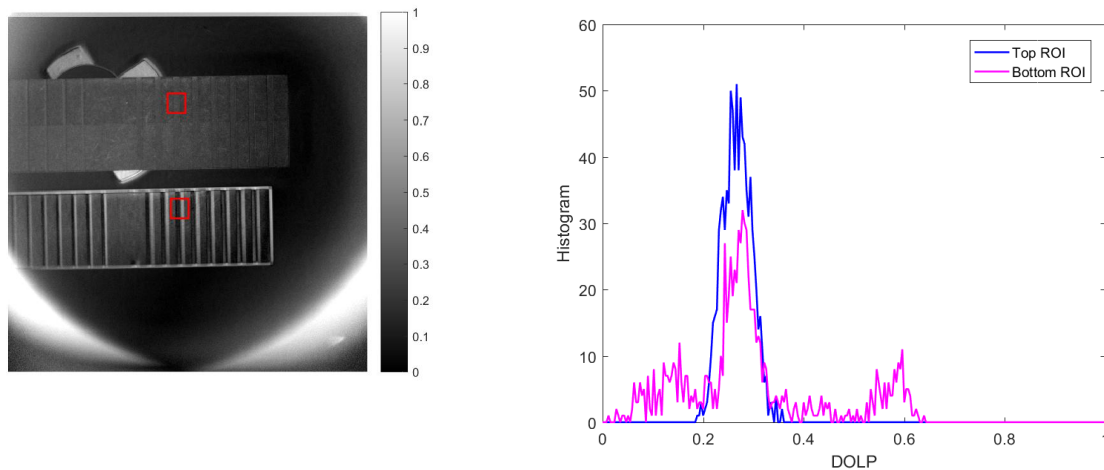


Figure 7: Example of $DOLP$ picture (left) focused on the sample on the top. Histograms (right) of the $DOLP$ on each of the two red ROIs defined on the $DOLP$ picture.

The difference between this two $DOLP$ histograms shows that at the right refocused distance, the $DOLP$ is more homogeneous, more tightened. To discriminate the histogram that is more tightened we base our estimation on the standard deviation (STD) which is a simple operator to characterize the width of a mono-mode histogram. We can then compute, for each ROI, the $DOLP$ STD for each refocused image of the stack. We obtain $DOLP$ STD curves depending on Z .

On Fig. 8 we show the STD curves of four different ROIs on a textured part of the image. One can see that the STD curves have minimum values. In fact, these minima correspond to the distance between the camera and the sample. If we define other ROIs on uniform surfaces, with no strong texture (see Fig. 9), it is interesting to observe that even if the STD curves have lower values, they still exhibit minima that correspond to the distance between the camera and the sample; at least for the top sample. In fact, the ROIs on the sample at the bottom, which is further away from the camera than the top sample, show STD curves that are fairly constant, with a minimum whose position is less obvious. We are reaching the limits of the STD-based method at this distance.

So far, we can conclude that the $DOLP(Z)$ provides enough information to distinguish uniform surfaces from marked surfaces, which may represent an appearance defect. In this last case, the position of the STD minimum also give information about the distance between the camera and this defect. And, in uniform case, if the sample

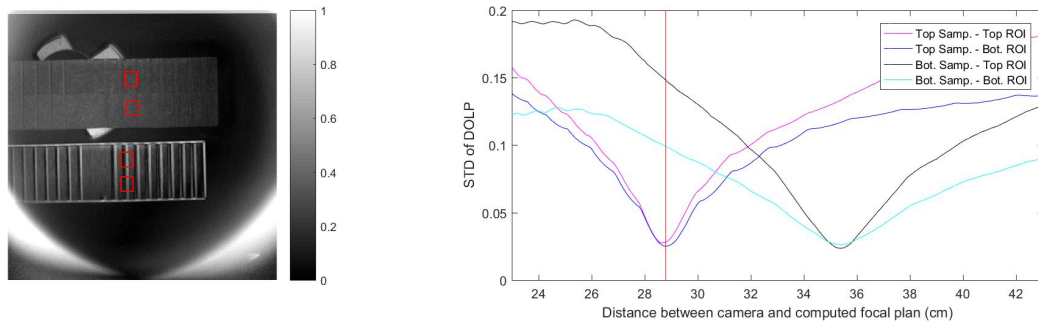


Figure 8: Video2 (online version) showing evolution of the standard deviation (right) of the *DOLP* along the computed depth, on four ROIs defined on the *DOLP* picture (left). <http://dx.doi.org/10.1117/12.2302592>

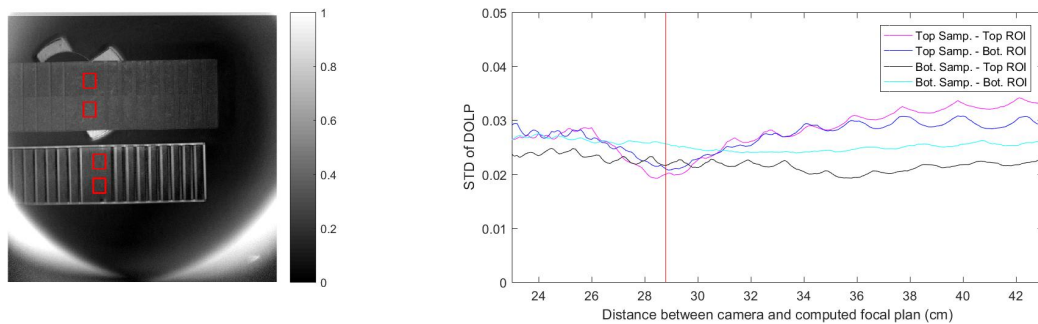


Figure 9: Video3 (online version) showing evolution of the standard deviation (right) of the *DOLP* along the computed depth, on four ROIs defined on the *DOLP* picture (left). <http://dx.doi.org/10.1117/12.2302592>

provides enough natural roughness and if the camera has sufficient resolution to detect it, the STD curve also provides the distance between the camera and the sample.

5.3 Analysis on limits of detection

At a distance of at least 35 cm to the camera, we know that we can detect tags or defects in the mm range. Now, if they are thinner, one can wonder if the system would still be able to detect them. In order to have an general idea about the defect detection accuracy, we have performed a third experiment where we examine a thin strip (0.1 mm wide), which is comparable to a slight appearance defect. This strip has been duplicated on the middle of both samples. As previously, we defined four ROIs and plotted the *DOLP* STD evolution for each ROI. The results are presented Fig. 10.

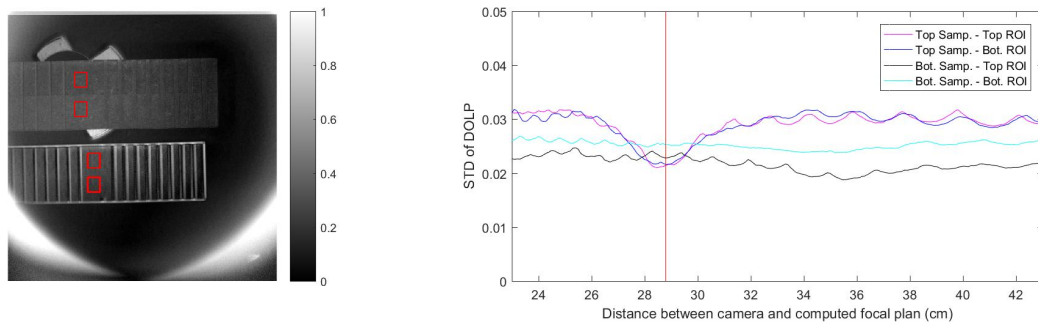


Figure 10: Video4 (online version) showing evolution of the standard deviation (right) of the *DOLP* along the computed depth, on four ROIs defined on the *DOLP* picture (left). <http://dx.doi.org/10.1117/12.2302592>

Looking at the overall STD evolution, we see that the curves exhibit the same general behavior as for smooth surfaces Fig. 9: For the top sample, we can identify a minimum that correspond to the distance between the sample and the camera, and for the bottom sample, it is hard to identify the exact position of the minimum. But when looking closely at the plots for the ROIs on the top sample, we can notice that the STD curves reach higher values for the thin defect than previously for smooth surfaces. To make this difference more noticeable, it is now interesting to compare STD curves on a different way. Up to now, STD were plotted on the same graph depending on the characteristics of the surface they referred to (smooth surfaces on the same graph, wide defect on the same graph). Now, we will group STDs differently, in a way that emphasizes the influence of the defect width. The result is presented Fig. 11. This figure presents, on each plot, three STDs that refers to the same global surface state (laser abraded surface, or original surface), but with different defect characteristics.

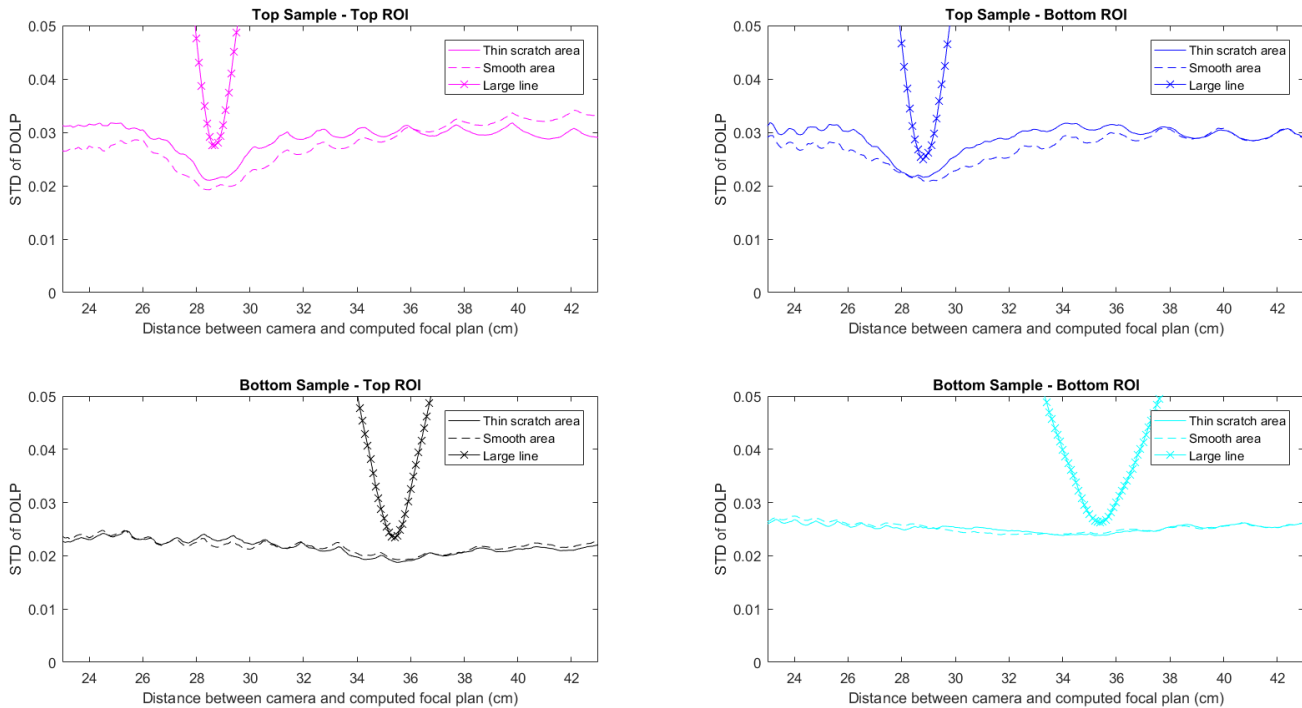


Figure 11: Evolution of the standard deviation of the *DOLP* along the computed depth, on all the previously studied ROIs. Note that the scales of the ordinate axis have voluntarily been defined at values that allow to compare the STD for the smooth area and the thin scratch area. The STD for the large line is then only partially drawn as it takes higher values.

First, let's analyze the STD curves for the top sample, on Fig. 11. These curves bring enough information to make the difference between a smooth surface, a thin scratch, or a larger stripe. We find again minima on all of the curves that give us the focusing distance. Moreover, when looking on a neighborhood of ± 5 cm around this focusing distance, we see that the STD curve for the thin scratch has higher values and steeper slopes than for the smooth surface. In a similar manner, but with much higher values, the STD for the large defect also exhibit higher values and steeper slopes than for the two other ROIs. To sum up: The higher and the steeper the STD, the wider the defect.

Now, let's have a look at the STD curves for the sample at the bottom that is further away from the camera. Here, we cannot make anymore difference between the smooth surface and the thin scratch. Moreover, no minimum can be clearly located on the curves to give camera to sample distance information. Only the large stripe exhibits STDs that are strongly different from the others. This means that as the sample goes further away from the camera, small defects will not be identified anymore.

As a conclusion, we can say that in the particular case of the wooden samples we used at a distance close enough to the camera (closer than 30 cm, approximately), we can:

- Retrieve the distance between the camera and the sample, not matter if there are defects or not
- Identify the presence of defects at least 0.1 mm wide, and give their distance to the camera

However, as the sample goes further away from the camera, only fairly large defects disrupt enough the *DOLP* information for the system to be able to identify both the presence of the defect and its distance to the camera. In case of smooth surfaces or thin scratches, neither the presence of a defect nor the distance between the sample and the camera can be identified. We are here reaching the limits of the system performances.

5.4 Comments on the results

On Fig. 9, when observing the STD for surfaces without apparent defects, flat STD curves could have been expected, showing that the *DOLP* would not vary with respect to the depth Z . However, we saw that the *DOLP* did vary significantly, at least for one of the two samples. This phenomenon can be explained by the nature of the material that is observed. As the wooden plates have fairly rough surfaces, they present small facets all over the ROIs. Therefore, when computing the *DOLP* on a uniform area, we observe the same phenomenon as the one generated by a stripe.

We also saw in the previous sections that for the sample that is further away from the camera, it is neither possible to discriminate a uniform surface and a thin scratch, nor to give the right focusing distance between the camera and the object if there is no strong defects within the ROI. This is due to optical aspects of the system. As objects go further away from the camera, the images acquired by the camera show less geometrical details of the sample. Therefore the surface seems smoother, and the STD curve is flatter.

6. CONCLUSION AND PERSPECTIVES

We have introduced a prototype of camera combining light field and polarimetric imaging. We have shown that the data captured can be used to compute a stack of images representing the *DOLP* allowing the Z direction. *DOLP*(Z) images can then be used to compute both depth and degree of linear polarization of samples analyzed by our system. The proof of concept has been shown by using two wooden samples where stripes of different widths had been machined by a laser beam. At a working distance of about 30 cm, we have shown that defects larger than few hundred microns can be detected, providing at the same time its distance to the camera and the *DOLP* of the damaged surface. Moreover, for any surfaces, which are exhibiting a relative roughness, the *DOLP*(Z) can also provides enough information to determine the distance between the camera and the sample, even when the surface doesn't have any particular defect. Further work will be devoted to studying materials of different natures such as plastic or metallic materials for various surface conditions. We will also model the system to define and understand the limits of this new imaging system.

REFERENCES

- [1] Vannier, N., Goudail, F., Plassart, C., Boffety, M., Feneyrou, P., Leviandier, L., Galland, F., and Bertaux, N., "Comparison of different active polarimetric imaging modes for target detection in outdoor environment," *Appl. Opt.* **55**(11), 2881–2891 (2016).
- [2] Terrier, P., Devlaminck, V., and Charbois, J. M., "Segmentation of rough surfaces using a polarization imaging system," *J. Opt. Soc. Am. A* **25**(2), 423–430 (2008).
- [3] Tyo, J. S., Goldstein, D. L., Chenault, D. B., and Shaw, J. A., "Review of passive imaging polarimetry for remote sensing applications," *Appl. Opt.* **45**(22), 5453–5469 (2006).
- [4] Gendre, L., Foulonneau, A., and Bigué, L., "Full stokes polarimetric imaging using a single ferroelectric liquid crystal device," *Optical Engineering* **50**, 50 – 50 – 10 (2011).
- [5] Marconnet, P., Gendre, L., Foulonneau, A., and Bigué, L., "Cancellation of motion artifacts caused by a division-of-time polarimeter," (2011).

- [6] Pezzaniti, J. L. and Chenault, D. B., “A division of aperture mwir imaging polarimeter,” *Proc.SPIE* **5888**, 5888 – 5888 – 12 (2005).
- [7] Andreou, A. G. and Kalayjian, Z. K., “Polarization imaging: principles and integrated polarimeters,” *IEEE Sensors Journal* **2**(6), 566–576 (2002).
- [8] Lippmann, G., “Épreuves réversibles donnant la sensation du relief,” *J. Phys. Theor. Appl.* **7**(1), 821–825 (1908).
- [9] Adelson, E. H. and Wang, J. Y. A., “Single lens stereo with a plenoptic camera,” *IEEE Transactions on Pattern Analysis and Machine Intelligence* **14**(2), 99–106 (1992).
- [10] Ng, R., *Digital Light Field Photography*, phd thesis, Stanford University, CA, USA (2006).
- [11] Levin, A., Fergus, R., Durand, F., and Freeman, W. T., “Image and depth from a conventional camera with a coded aperture,” *ACM Trans. Graph.* **26**(3) (2007).
- [12] Wilburn, B., Joshi, N., Vaish, V., Talvala, E.-V., Antunez, E., Barth, A., Adams, A., Horowitz, M., and Levoy, M., “High performance imaging using large camera arrays,” *ACM Trans. Graph.* **24**(3), 765–776 (2005).
- [13] Lumsdaine, A. and Georgiev, T., “The focused plenoptic camera,” in [*Computational Photography (ICCP), 2009 IEEE International Conference on*], 1–8, IEEE (2009).
- [14] Fu, W., Tong, X., Shan, C., Zhu, S., and Chen, B., “Implementing light field image refocusing algorithm,” in [*2015 2nd International Conference on Opto-Electronics and Applied Optics (IEM OPTRONIX)*], 1–8 (2015).
- [15] Lytro, “Lytro cinema,” (2018).
- [16] Tao, M. W., Hadap, S., Malik, J., and Ramamoorthi, R., “Depth from combining defocus and correspondence using light-field cameras,” in [*Proceedings of the 2013 IEEE International Conference on Computer Vision*], *ICCV '13*, 673–680, IEEE Computer Society, Washington, DC, USA (2013).
- [17] Georgiev, T., Lumsdaine, A., and Chunev, G., “Using focused plenoptic cameras for rich image capture,” *IEEE Computer Graphics and Applications* **31**(1), 62–73 (2011).
- [18] Horstmeyer, R., Athale, R., and Euliss, G., “Modified light field architecture for reconfigurable multimode imaging,” **7468** (2009).
- [19] Xiao, X., Javidi, B., Saavedra, G., Eismann, M., and Martinez-Corral, M., “Three-dimensional polarimetric computational integral imaging,” *Opt. Express* **20**(14), 15481–15488 (2012).
- [20] Carnicer, A. and Javidi, B., “Polarimetric 3d integral imaging in photon-starved conditions,” *Opt. Express* **23**(5), 6408–6417 (2015).
- [21] Riou, C., Colicchio, B., Lauffenburger, J., and Cudel, C., “Interests of refocused images calibrated in depth with a multi-view camera for control by vision,” in [*Thirteenth International Conference on Quality Control by Artificial Vision, QCAV 2017, Tokyo, Japan, May 14, 2017*], 1033807 (2017).
- [22] Stokes, G., “On the composition and resolution of streams of polarized light from different sources,” *Transactions of Cambridge Philosophical Society* **9**, 339–416 (1852).
- [23] Goldstein, D., [*Polarized Light*], Marcel Dekker, New York & Basel, second ed. (2003).